Journal of Nuclear Medicine, published on June 26, 2025 as doi:10.2967/jnumed.125.270165

Quantitative Measurement of Tau Burden in a Dual-Time-Window Dynamic PET Imaging Protocol with [^{18}F]MK6240

Ye Xia*[1,2], Maeva Dhaynaut*[3], Yanis Chemli[3], Cristina Lois[1], Bernard J. Hanseeuw[1,4], Emma Thibault[1], Colin Groot[2,5], Rik Ossenkoppele[2,5,6], Keith Johnson[1], Georges El Fakhri[3,7], Marc D. Normandin[3], and Nicolas J. Guehl[3]

[1]*Department of Radiology, Massachusetts General Hospital, Harvard Medical School, Boston, Massachusetts;* [2]*Alzheimer Center Amsterdam, Department of Neurology, Vrije Universiteit Amsterdam, Amsterdam UMC location VUmc, Amsterdam, The Netherlands;* [3]*Department of Radiology and Biomedical Imaging, Yale School of Medicine, New Haven, Connecticut;* [4]*Department of Neurology, Cliniques Universitaires Saint-Luc, Université Catholique de Louvain, Brussels, Belgium;* [5]*Neurodegeneration, Amsterdam Neuroscience, Amsterdam UMC, Amsterdam, The Netherlands;* [6]*Clinical Memory Research Unit, Lund University, Lund, Sweden; and* [7]*Department of Biomedical Informatics and Data Science, Yale School of Medicine, New Haven, Connecticut*

This study aimed to test and validate a dual-time-window (DTW) protocol for 6-(fluoro-^{18}F)-3-(^{1}H-pyrrolo[2,3-c]pyridin-1-yl)isoquinolin-5-amine ([^{18}F]MK6240) dynamic PET imaging in experimental datasets acquired in human subjects. **Methods:** DTW protocols were tested and validated in datasets previously collected in 25 participants: 13 were cognitively normal, 10 had mild cognitive impairment, and 2 had Alzheimer disease. Participants underwent full 120-min [^{18}F]MK6240 dynamic PET scans as well as structural MRI. Intermediary 3-dimensional volumes were removed from the acquired dynamic PET images to emulate DTW acquisitions consisting of an early phase and a late phase. Five break durations (30, 40, 50, 60, and 70 min) were investigated to determine the optimal break for 2 study durations (120 and 110 min). Regional brain time–activity curves were extracted using atlases available in the Montreal Neurologic Institute template space and using the FreeSurfer parcellation. Interpolation strategies were tested to recover the missing time points. Distribution volume ratio (DVR) estimates obtained from the DTW time–activity curves were compared with those obtained from the full time–activity curves as reference. Parametric maps were generated for the selected protocol and evaluated. **Results:** The correlation and agreement between DVR values obtained from the DTW method and the full time–activity curves were overall very good. The DTW protocol with a 60-min break using a biexponential model fit as the interpolation method provided the best compromise between practicality and quantitative accuracy. The mean differences between this DTW and the full acquisition, averaged across brain regions and all subjects, were less than 1% with a corresponding SD of less than 4%, and DVR estimates were not statistically different from those obtained from the full acquisition ($P > 0.05$). DVR parametric images were visually and quantitatively consistent with those obtained from the full acquisition. **Conclusion:** This study presents strong support for the use of a DTW protocol with [^{18}F]MK6240. Such a protocol would be well suited to allow for both quantification of tau and derivation of an index of cerebral perfusion while reducing patient discomfort and increasing scanning efficiency in comparison to a full dynamic acquisition.

Key Words: [^{18}F]MK6240; dual-time-window imaging; tau imaging; PET; Alzheimer disease

Received Apr. 11, 2025; revision accepted May 21, 2025.

For correspondence or reprints, contact Nicolas J. Guehl (nicolas.guehl@yale.edu).

*Contributed equally to this work.

Published online Jun. 18, 2025.

J Nucl Med 2025; 00:1–8
DOI: 10.2967/jnumed.125.270165

The radiotracer 6-(fluoro-^{18}F)-3-(^{1}H-pyrrolo[2,3-c]pyridin-1-yl)isoquinolin-5-amine ([^{18}F]MK6240) was developed for in vivo imaging and quantification of hyperphosphorylated tau (*1*,*2*), a key neuropathologic hallmark of Alzheimer disease (AD). [^{18}F]MK6240 is one of the most characterized tau tracers to date (*3*–*10*). It has been extensively used in research studies and is also currently being used in clinical trials testing disease-modifying therapeutic agents against AD (*11*). Recent studies demonstrated that the early phase of [^{18}F]MK6240 dynamic PET imaging can provide valuable information on cerebral perfusion, thus potentially offering complementary information to the measurement of tau load obtained with this tracer (*12*,*13*). Since cerebral blood flow and brain metabolism are coupled, this early phase may also be viewed as a potential surrogate for [^{18}F]FDG imaging to inform on patterns of neurodegeneration as previously proposed by other investigators for other tau and amyloid PET tracers (*14*–*19*).

Although a full dynamic PET acquisition is ideal for obtaining both quantitative measurements of tau burden and an index of cerebral perfusion, such long dynamic scanning protocols are impractical in clinical settings and may result in patient discomfort and low scanning efficiency. Consequently, late static [^{18}F]MK6240 scans may be preferred and the SUV ratio (SUVR) calculated, typically using imaging windows of 90–110 min or 90–120 min after tracer injection, as a surrogate measure of tau burden. However, although late SUVR correlates well with the quantitative distribution volume ratio (DVR) obtained with dynamic scan protocols (*3*–*6*), this metric is only semiquantitative—that is, full equilibrium between the target and reference regions may not be completely achieved, particularly in high-binding target regions (*20*,*21*)—and may require strict adherence to the specified imaging time window, especially in longitudinal studies (*6*). More generally, SUVR may also be sensitive to changes in cerebral blood flow (*22*,*23*), thus potentially introducing another confounding effect in the quantification of tau. Lastly, late static scans cannot inform on cerebral perfusion, which can add useful information on brain function in clinical trials or for diagnosis and

staging following the amyloid/tau/neurodegeneration classification scheme (*24*–*26*).

Alternatively, previous works have demonstrated the usefulness and practicality of dual-time-window (DTW) acquisition protocols for various PET tracers, including those that target amyloid and other tau tracers (*27*–*30*). Such protocols consist of an early imaging phase and a late imaging phase separated by a break during which the scanner can be used to interleave another imaging study. These protocols demonstrated a good compromise between a late static acquisition and a full dynamic acquisition while retaining good quantitative accuracy. Such protocols are, in theory, applicable for [^{18}F]MK6240 tau imaging and would allow both quantitative measurements of tau load and cerebral perfusion by tracer kinetic modeling. However, DTW protocols need to be validated and optimized on a tracer-by-tracer basis because of differences in pharmacokinetic properties. Recently, Kolinger et al. presented a pilot study toward the validation of a DTW protocol for [^{18}F]MK6240 using simulations (*31*). The authors generated noiseless [^{18}F]MK6240 brain time–activity curves based on kinetic parameters as well as arterial blood and plasma data obtained from a small subset of human studies. Although their results were encouraging, the authors acknowledged that additional validation studies are needed with larger cohorts.

The aim of the present work is to validate a DTW [^{18}F]MK6240 dynamic imaging protocol in datasets acquired in human subjects. We investigated different break durations and tested 2 interpolation methods to determine the optimal balance between quantitative accuracy and practicality in 2 different study duration (120 and 110 min). In addition, we applied the method at the voxel level to generate DVR parametric maps, evaluated their quantitative accuracy, and tested the feasibility of generating model-based SUVR images within the break.

MATERIALS AND METHODS

Participants

Only datasets consisting of a full dynamic [^{18}F]MK6240 acquisition (i.e., no break during the acquisition) were included in this work to serve as a reference. In total, 25 subjects, consisting of 13 who were cognitively normal (CN), 10 who had mild cognitive impairment (MCI), and 2 who had AD, were included. Two of the CN subjects also underwent a retest dynamic [^{18}F]MK6240 scan acquired within 3 wk of the first scan. All subjects were identified by physicians at Massachusetts General Hospital and underwent at least 1 comprehensive medical and neurologic evaluation using tests that included the Mini-Mental State Examination. Clinical status (MCI, AD, or CN) was determined clinically by established criteria (*32*). All subjects signed an informed-consent form, and the study was approved by the institutional review board at Massachusetts General Hospital.

Data Acquisition

Data acquisition, image reconstruction, and processing for extraction of regional brain time–activity curves were previously described in detail elsewhere (*12*) and are briefly summarized here. Each subject had a full 120-min dynamic PET scan that started immediately with the intravenous injection of [^{18}F]MK6240, as well as structural MRI with a T1-weighted magnetization-prepared rapid gradient-echo sequence for anatomic reference. Time bins used to frame the full 120-min PET emission data were 6 × 10 s, 8 × 15 s, 6 × 30 s, 8 × 60 s, 8 × 120 s, and 18 × 300 s bins. Subjects also underwent a 60-min dynamic [^{11}C]Pittsburgh compound B (PiB) PET scan to determine PiB score and amyloid status (*33*). Participants were scanned on a Discovery MI (GE HealthCare) PET/CT scanner (*34*). [^{18}F]MK6240 and [^{11}C]PiB were synthesized as previously described (*35*,*36*). Injected [^{18}F]MK6240 activities at the time of injection were 179.3 ± 12.4 MBq (range, 156.5–200.9 MBq). The molar activity of [^{18}F]MK6240 at the time of injection was 70.7 ± 56.6 GBq/μmol (range, 16.3–291.4 GBq/μmol). The total injected mass was 1,115.7 ± 847.8 ng (range, 176.0–3,165.9 ng), corresponding to 4.0 ± 3.0 nmol (range, 0.6–11.4 nmol).

Image Processing

As previously described in detail by Guehl et al. (*12*), each dynamic dataset was corrected for motion, PET and MR images were aligned, and regional brain time–activity curves were extracted from the full dynamic PET data using the Montreal Neurologic Institute (MNI) template space and the FreeSurfer parcellation (*37*). The MNI regions of interest (ROIs) surveyed in this work were the precuneus cortex, mesial temporal cortex, hippocampus, thalamus, frontal cortex, occipital cortex, parietal cortex, temporal cortex, white matter, and whole brain. FreeSurfer-derived ROIs are listed in Supplemental Table 1 (supplemental materials are available at http://jnm.snmjournals.org).

DTW dynamic images were created by removing intermediary 3-dimensional volumes from the motion-corrected reconstructed full dynamic images. Five break durations were tested (30, 40, 50, 60, and 70 min) while the time window of the late dynamic phase was kept to 90–120 min (i.e., corresponding to break intervals of 60–90, 50–90, 40–90, 30–90, and 20–90 min after tracer injection). A late time window of 90–110 min was also investigated by removing the last 10 min of the PET acquisition. The 2 dynamic segments were then concatenated to form a single dynamic dataset, and regional DTW time–activity curves were extracted using the same masks and FreeSurfer parcellation as for the set of full dynamic images. For reference, a 60-min break 120-min DTW protocol comprises an early-phase dynamic PET acquisition with corresponding time bins of 6 × 10 s, 8 × 15 s, 6 × 30 s, 8 × 60 s, and 8 × 120 s, followed by a 60-min break and a late-phase dynamic PET acquisition with corresponding time bins of 6 × 300 s. Other DTW protocols were obtained in a similar fashion, that is, by removing the PET volumes at relevant time bins.

Analysis of DTW Regional Time–Activity Curves

The missing PET data in the gap of the DTW time–activity curves (i.e., between the early and late dynamic phases) were interpolated using 2 methods: by simple linear interpolation as in Kolinger et al. (*31*) and by fitting a sum of 2 exponentials (i.e., in the form: $\mathrm{PET}(t) = A_1 e^{\lambda_1 t} + A_2 e^{\lambda_2 t}$, where t is time, A_1 and A_2 are amplitude terms, and λ_1 and λ_2 are decay constants) to the decreasing part of the DTW time–activity curves. The biexponential method was fitted starting 2 min after the peak to the end of the time–activity curve (i.e., to either 120 or 110 min), and the model fit was used to recover the gap of the DTW by interpolating at the missing time points. Supplemental Figure 1 shows examples of interpolated brain time–activity curves.

The Logan graphical method with a reference region input (*38*) was used to analyze the time–activity curves for direct estimation of DVR as a measure of tau load using the cerebellar gray matter as a reference region (*6*). DVR estimates obtained from the DTW time–activity curves were compared with those obtained from the full dynamic time–activity curves (i.e., either 0–120 or 0–110 min) as a reference.

Parametric Mapping

Dynamic [^{18}F]MK6240 images were smoothed with a gaussian filter of 4 mm in full width at half maximum, and parametric DVR images were computed using the Logan graphical method with a reference region input. DVR images were computed with the selected DTW protocol by applying the interpolation method to the reference region time–activity curve and to each voxel of the image. Resulting DVR images were compared with those computed from the full dynamic acquisition as a reference.

Model-Based SUVR Maps

Since several groups use a late static imaging window of 70–90 min for SUVR calculation ($SUVR_{70\text{-}90}$) (*3*,*39*,*40*), we also investigated whether model-based $SUVR_{70\text{-}90}$ images could provide accurate $SUVR_{70\text{-}90}$ estimates in light of a potential need for data harmonization across imaging sites. Briefly, the selected interpolation method was applied voxel by voxel to recover the missing volumes of the DTW dynamic images, and static model-based $SUVR_{70\text{-}90}$ images were computed from the corresponding recovered frames. The resulting model-based $SUVR_{70\text{-}90}$ images were compared with the original $SUVR_{70\text{-}90}$ images (i.e., generated from the acquired data).

Statistical Analysis

Scatterplots with total least squares regressions were presented along with the line of identity to indicate the correlation between DVR measurements obtained from the DTW method and the full acquisition. Bland–Altman plots were used to assess agreement between DVR measurements. The Pearson correlation coefficient, *r,* was used to assess the strength of the total least squares linear regressions. All data were expressed as mean value ± SD unless otherwise specified. Paired 2-tailed *t* testing assuming equal variance was used to compare regional DVR and SUVR values between the DTW protocol and the full acquisition. A *P* value of 0.05 or less was considered statistically significant. Bonferroni adjustment was applied for multiple comparisons within the same datasets when appropriate. In the 2 CN subjects with retest acquisition, test–retest (T-RT) reliability was calculated as $\%T\text{-}RT = 100 \times 2x\,|(test - retest|/(test + retest)$.

RESULTS

Participant Demographics

Subject demographics are shown in Table 1. CN subjects ($n = 13$) had a Mini-Mental State Examination ranging from 25 to 30. The other subjects were classified as having MCI or AD according to the National Institute of Aging research criteria. Eleven subjects (3 CN, 6 MCI, and 2 AD) were amyloid-positive as defined by a [^{11}C]PiB DVR greater than 1.2 calculated in a large cortical ROI (frontal, lateral temporal, and retrosplenial cortices) (*33*). The CN and MCI/AD groups were well matched in age (65.2 ± 13.2 y vs. 69.4 ± 8.1 y, $P = 0.3526$; unpaired 2-sample *t* test).

Comparison of Regional DVR Estimates Between DTW and Full Time–Activity Curves

Overall, for both the 120-min and the 110-min study durations, the biexponential method applied to DTW acquisitions provided DVR estimates that were highly correlated and in very good agreement with DVR values obtained from the full dynamic acquisition (Supplemental Figs. 2A–2E and 3A–3E for the FreeSurfer analysis; Supplemental Figs. 4A–4E and 5A–5E for the MNI analysis). With the exception of the 70-min break in the FreeSurfer analysis, all other breaks showed a mean difference, as calculated across all brain regions and subjects, smaller than 1%, with a corresponding SD smaller than 4%. Those DVR estimates were not statistically different from those obtained from the full acquisition ($P > 0.05$). The 70-min break, however, showed slightly increased variability in the Bland–Altman plots, and differences in DVR were statistically significant for both study durations and analysis methods ($P < 0.05$) (Supplemental Figs. 2E, 3E, 4E, and 5E).

In contrast, whereas the DTW protocol using linear interpolation showed a strong correlation and good agreement in DVR values for the 30- and 40-min breaks, its performance tended to decrease as break duration increased (Supplemental Figs. 2F–2J and 3F–3J for the FreeSurfer analysis; Supplemental Figs. 4F–4J and 5F–5J for the MNI analysis). Indeed, the slope of the total least squares regressions became gradually lower than unity, and trends in Bland–Altman plots became more pronounced with increasing break duration. Altogether, these results indicated that the biexponential method with a DTW protocol consisting of a 60-min break may provide the best compromise between quantitative accuracy and practicality (i.e., the longest break providing DVR estimates equivalent to those derived from full dynamic scans). Figures 1 and 2 show the correlation and Bland–Altman plots for the 60-min DTW protocol using biexponential fits for the 120- and 110-min scan analyses, respectively. Analyses performed

TABLE 1
Participant Demographics and Clinical Characteristics

Characteristic	All	MCI/AD grouped	CN	MCI	AD
Total patients (*n*)	25	12	13	10	2
Age (y)	67.2 (11.0)	69.4 (8.1)	65.2 (13.2)	71.0 (7.8)	61.5 (4.9)
Weight (kg)	82.5 (19.2); 1*	79.6 (18.4); 1*	85.1 (20.3)	82.5 (18.0); 1*	66.5 (19.6)
Sex (*n*)					
Male	15	8	7	7	1
Female	10	4	6	3	1
MMSE	26.0 (4.4)	23.3 (5.0)	28.4 (1.4)	25.2 (2.6)	14.0 (1.4)
MMSE range	13–30	13–29	25–30	21–29	13–15
Education (y)	16.1 (2.8)	16.6 (3.1)	15.7 (2.7)	16.2 (3.2)	18.5 (2.1)
PiB status (*n*)					
Positive	11	8	3	6	2
Negative	14	4	10	4	0

*Number of participants for which information was not available.
MMSE = Mini-Mental State Examination.
Data in parenthesis are SD.

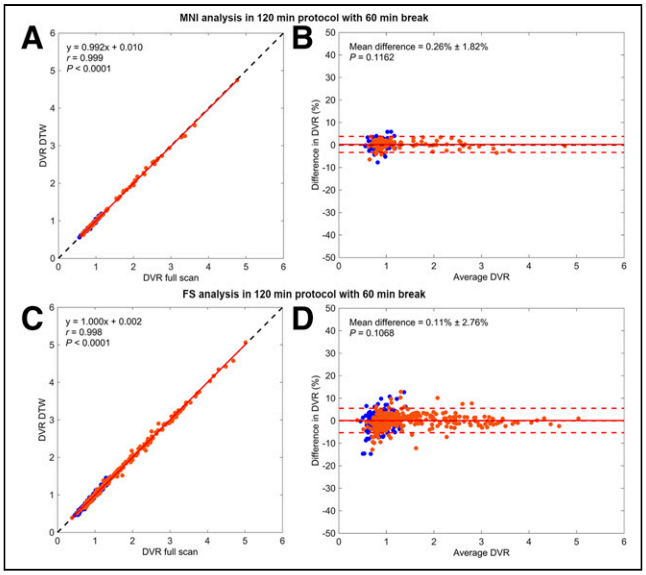

FIGURE 1. Comparison of DVR estimates computed for 60-min break in 120-min scan analysis with biexponential fit with DVR estimates obtained from full 120-min scan duration. (A and B) Correlation and modified Bland–Altman plots of DVR estimates for analysis performed using atlases from MNI template space. (C and D) Correlation and modified Bland–Altman plots of DVR estimates for analysis performed using FreeSurfer parcellation. In correlation plots (A and C), solid red lines represent total least squares regressions and black dashed lines are lines of identity. In Bland–Altman plots (B and D), solid red lines represent mean differences, dashed red lines show mean differences ± 1.96 SDs, and black dashed lines are zero lines for references. Blue dots represent CN subjects, and orange dots represent MCI/AD subjects. Data points are for all subjects and regional brain time–activity curves. FS = FreeSurfer.

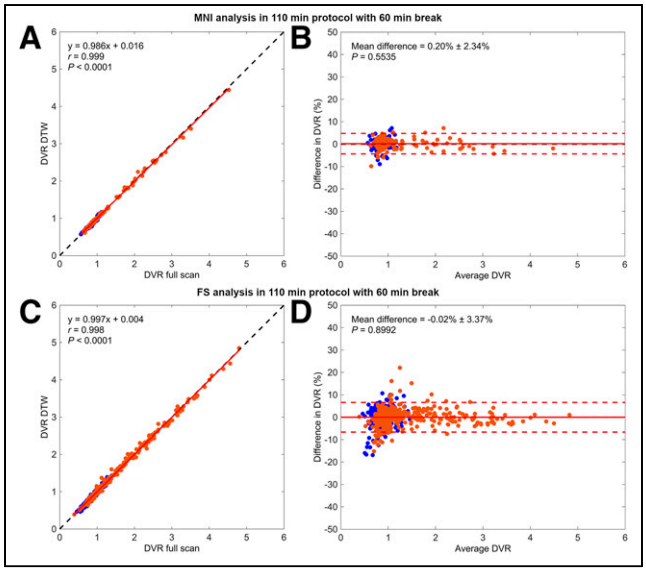

FIGURE 2. Comparison of DVR estimates computed for 60-min break in 110-min scan analysis with biexponential fit with DVR estimates obtained from full 110-min scan duration. (A and B) Correlation and modified Bland–Altman plots of DVR estimates for analysis performed using atlases from MNI template space. (C and D) Correlation and modified Bland–Altman plots of DVR estimates for analysis performed using FreeSurfer parcellation. In correlation plots (A and C), solid red lines represent total least squares regressions and black dashed lines are lines of identity. In Bland–Altman plots (B and D), solid red lines represent mean differences, dashed red lines show mean differences ± 1.96 SDs, and black dashed lines are zero lines for references. Blue dots represent CN subjects, and orange dots represent MCI/AD subjects. Data points are for all subjects and regional brain time–activity curves. FS = FreeSurfer.

using atlases from the MNI template space and those using the FreeSurfer parcellation both indicated a strong correlation and a very good agreement between the DVR of that DTW protocol and the DVR from the full dynamic PET acquisition. As expected, the analyses using the FreeSurfer parcellation demonstrated slightly more variability than did the analyses using the MNI atlases, likely because of the increased number of small ROIs. Likewise, the 110-min scan analysis demonstrated slightly more variability in DVR estimates than the 120-min scan analysis for both the FreeSurfer parcellation (mean difference, −0.02% ± 3.37% vs. 0.11% ± 2.76%) and the comparison using the MNI atlases (mean difference, 0.20% ± 2.34% vs. 0.26% ± 1.82%), likely because the method relies on less dynamic data. For completeness, the comparisons between DVR estimates computed for the 60-min break in the 110-min scan analysis with biexponential fit and DVR estimates obtained from the full 120-min scan duration are shown in Supplemental Figure 6.

Region-by-region differences in DVR estimates obtained for the 120- and 110-min scan analyses for the FreeSurfer parcellation are presented in Supplemental Tables 1 and 2. Statistically significant differences were observed in only a few regions, notably for the CN group; however, most of those differences did not survive after Bonferroni adjustment. Overall, these results demonstrate that the 60-min DTW protocol using the biexponential fit provides accurate DVR estimates.

T-RT Studies

Figure 3 and Supplemental Figure 7 show the T-RT variability obtained with the different break durations (30, 40, 50, 60, and 70 min) tested in this work and the T-RT variability of the full-scan analyses for reference. Our results were consistent between the 120- and 110-min scan analyses and on average indicated T-RT performance comparable to the full scan for all break durations, except for the 70-min break protocol, which showed increased variability notably in the FreeSurfer analyses. The linear interpolation method provided overall similar T-RT performance but slightly less variability in the 70-min break protocol (Supplemental Fig. 8).

These results demonstrated that, in addition to providing the best compromise between quantitative accuracy and practicality, the biexponential method with a 60-min break DTW protocol also provides precise quantification. Therefore, this protocol was selected as the method of choice for the computation of parametric maps and model-based SUVR maps.

Parametric Imaging

Figures 4 and 5 show DVR parametric maps computed for the 120- and 110-min scan analyses, respectively, along with the structural MR images, and DVR images computed from the full dynamic acquisition for reference. Visually, the parametric DVR images generated from the DTW protocol closely resembled those obtained from the full dynamic scan. The difference maps showed only small differences inside the brain, and most of the differences were actually observed in extracerebral structures where off-target binding has been reported for this tracer (meninges, ethmoid sinus, retina) (*3*,*6*). Comparisons of regional DVR values between the DTW and full-scan parametric maps demonstrated strong correlations and good agreements despite some overestimation by the

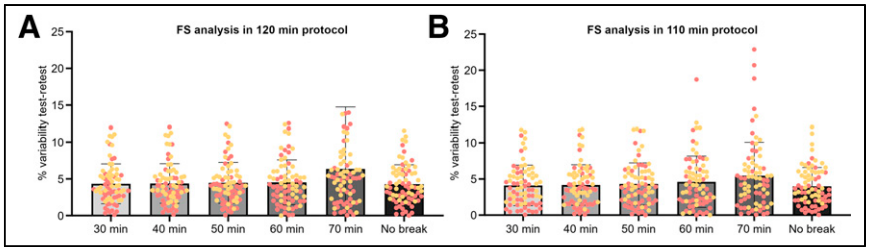

FIGURE 3. T-RT variability in 2 CN subjects for different break durations (30, 40, 50, 60, and 70 min) of DTW protocol with biexponential fit, compared with full scan acquisition (no break). (A) T-RT performance for 120-min scan analysis. (B) T-RT performance for 110-min scan analysis. (A and B) Analyses performed using FreeSurfer parcellation. Analyses performed using atlases from MNI template space are in Supplemental Figure 10. Each data point represents a brain region surveyed in this study. Yellow and orange dots correspond to regional data for 2 different CN subjects. In panel B, 2 data points for 70-min break condition do not appear on graph as they lie outside graph limits. FS = FreeSurfer.

DTW maps, which was more pronounced in the 110-min scan analysis (Supplemental Figs. 9 and 10).

Model-Based SUVR Maps

Figures 6 and 7 show model-based $SUVR_{70\text{-}90}$ images computed with the 60-min break DTW protocol for the 120- and 110-min scan analyses, respectively, along with the structural MR images, and the original $SUVR_{70\text{-}90}$ images for reference. Overall, the model-based images were visually consistent with the original $SUVR_{70\text{-}90}$ images, and regional comparisons demonstrated good quantitative accuracy (Supplemental Figs. 11 and 12).

DISCUSSION

In this work, we evaluated different DTW imaging protocols for [^{18}F]MK6240 using datasets acquired in CN, MCI, and AD participants, focusing on their impact on DVR quantification. We performed our investigation for 2 study lengths (120 and 110 min), testing different break durations—ranging from 30 to 70 min by an increment of 10 min—and 2 interpolation methods to recover the missing data: a simple linear interpolation and a biexponential model. We used the full dynamic datasets as a reference to evaluate the accuracy of the DVR estimates derived from the DTW protocols, and we aimed to select the protocol providing the best compromise between practicality in a clinical setting (i.e., maximizing break duration) and quantitative accuracy. We first performed our evaluation for regional analyses (i.e., at the ROI level) using atlases from the MNI template as well as the FreeSurfer parcellation, and then we computed DVR parametric maps using the selected DTW protocol.

Regional Quantification of DVR

Our results showed that both interpolation methods were quantitatively accurate for relatively small breaks (30 and 40 min), but the biexponential method outperformed the simple linear interpolation for larger breaks—that is, when the tracer distribution is changing significantly during the break. This finding was expected, and the choice of a biexponential function is consistent with the fact that the kinetics of [^{18}F]MK6240 are best described by a 2-tissue compartmental model (*4*,*6*). In fact, DTW protocols using the biexponential fit and breaks shorter than or equal to 60 min provided DVR values that were not statistically different from those obtained from the full acquisition. Moreover, our T-RT studies performed on 2 CN subjects suggested that those DTW protocols were also precise in low-binding brain regions. Altogether, these findings led us to select the 60-min break DTW protocol with biexponential fitting as the best compromise between quantitative performance and practicality. It should be noted, however, that the selection of a given DTW protocol may be driven by the application and underlying goal of a particular study (i.e., according to the level of quantitative accuracy needed in a given setting). The selection of a preferred break duration of 60 min is consistent with the study of Kolinger et al., who also selected a DTW protocol with a 60-min break as their optimal protocol, but our works present some differences and complementary results (*31*). First, their work was based solely on simulations, where noiseless time–activity curves were derived from human datasets acquired in only 8 subjects. Second, their range of DVR spanned values up to 3 (up to 5 in the present work). Third, they used only linear interpolation to recover the missing data in the DTW break.

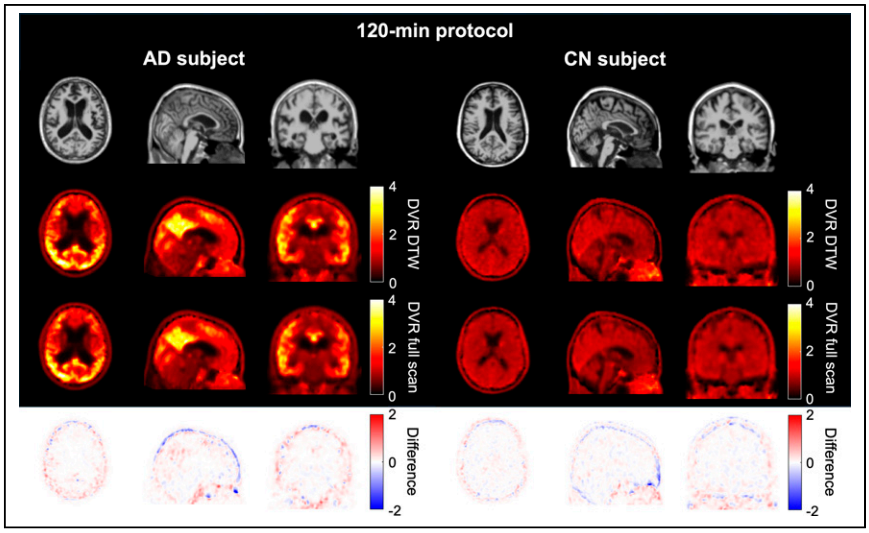

FIGURE 4. DVR maps computed for 60-min break with biexponential fit and 120-min scan analysis, and corresponding MR structural images in AD subject and CN subject. First row shows magnetization-prepared rapid gradient echo MRI for anatomic reference. Second row shows parametric DVR images generated from DTW images. Third row shows parametric DVR images generated from full 120-min dynamic images for comparison. Fourth row shows images of difference (DVR DTW – DVR full scan).

Parametric Mapping and Model-Based SUVR Images

The DTW protocol provided DVR parametric maps that were visually consistent with those obtained from the full dynamic scans, and regional analyses of those parametric

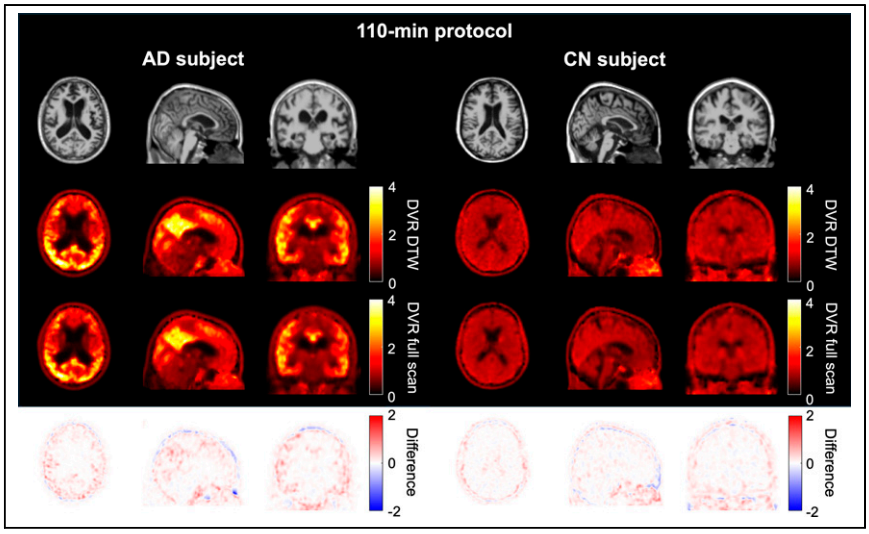

FIGURE 5. DVR maps computed for 60-min break with biexponential fit and 110-min scan analysis, and corresponding MR structural images for same AD and CN subjects as shown in Figure 4. First row shows magnetization-prepared rapid gradient echo as anatomic reference. Second row shows parametric DVR images generated from DTW images. Third row shows parametric DVR images generated from full 110-min dynamic images for comparison. Fourth row shows images of difference (DVR DTW – DVR full scan).

maps demonstrated strong correlations in DVR values despite some slight overestimation, which was more apparent at increasing DVR values—that is, in brain regions with slower kinetics (in high-binding brain regions of MCI/AD subjects). This observation is likely related to the artificially reduced statistical noise level in the DTW voxel time–activity curves (i.e., compared with the original full acquisition) due to using the model fits to recover the missing data. Thus, this finding is consistent with the notion that Logan plots are known to suffer from a noise-induced negative bias that is more pronounced in high-binding regions than in low-binding regions (*41*). Lastly, we also showed that the biexponential model can be used to predict $SUVR_{70\text{-}90}$ images with good quality and accuracy. Such surrogate $SUVR_{70\text{-}90}$ images may be useful for post hoc multicenter analyses when pooling datasets with institutions using such static time window protocols.

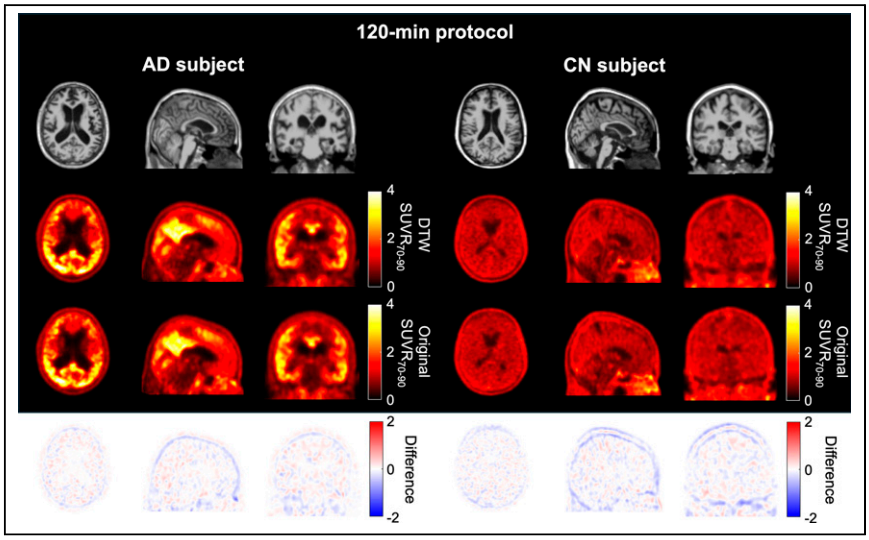

FIGURE 6. Model-based $SUVR_{70\text{-}90}$ maps computed for 60-min break with biexponential fit and 120-min scan analysis as well as corresponding MR structural images for same AD and CN subjects as shown in Figure 4. First row shows magnetization-prepared rapid gradient echo as anatomic reference. Second row shows parametric $SUVR_{70\text{-}90}$ images generated from DTW images. Third row shows original (i.e., from acquired data) $SUVR_{70\text{-}90}$ images for comparison. Fourth row shows images of difference ($SUVR_{70\text{-}90}$ DTW – $SUVR_{70\text{-}90}$ original).

Limitations

Our study presents some limitations. First, the dynamic DTW datasets used in this work were not directly acquired as such but were obtained post hoc by removing intermediary 3-dimensional volumes from the full dynamic PET acquisitions. Although this strategy enabled us to use the full dynamic PET acquisitions as reference for validation, it does not necessarily fully replicate the experimental conditions of an actual DTW protocol. For instance, in practice, some degree of misalignment would occur between the early and late dynamic segments of the DTW acquisition because of the subject's repositioning between the 2 acquisition phases. Although an accurate late-PET–to–early-PET registration may be challenging because of the widely different tracer distribution between the 2 acquisition phases, the 2 low-dose CT scans—which would be required for attenuation correction of each PET segment—could be used for registration purposes as well. Such registration should be relatively straightforward and robust; however, future works may include assessing the impact of such a procedure on the quantitative DVR measurements. Another limitation relates to potential physiologic changes—such as variations in cerebral blood flow—due to a subject's moving between the acquisition of the 2 DTW phases as opposed to staying still on the scanner bed during a full acquisition. In practice, this would be no different from late static imaging protocols if SUVR is used as a semiquantitative index to quantify tau burden. Likewise, although standard kinetic modeling techniques typically assume the physiologic system to be in steady state during the entire dynamic acquisition, DVR measurements should not be affected by such cerebral blood flow changes, as this metric is typically insensitive to changes in tracer delivery. Moreover, since our group previously demonstrated that only a few minutes are required to obtain a surrogate measure of cerebral perfusion, those measurements would be derived directly from the early-phase dynamic PET segment and would not be affected either (*12*). Lastly, our datasets included a total of 25 subjects, with approximately half classified as MCI/AD but only 2 as AD. Although our sample size was relatively small, we chose to include only subjects with a full—that is, uninterrupted—dynamic acquisition for reference to avoid potential biases or limitations that may be introduced by partial datasets. Nonetheless, these datasets covered a broad

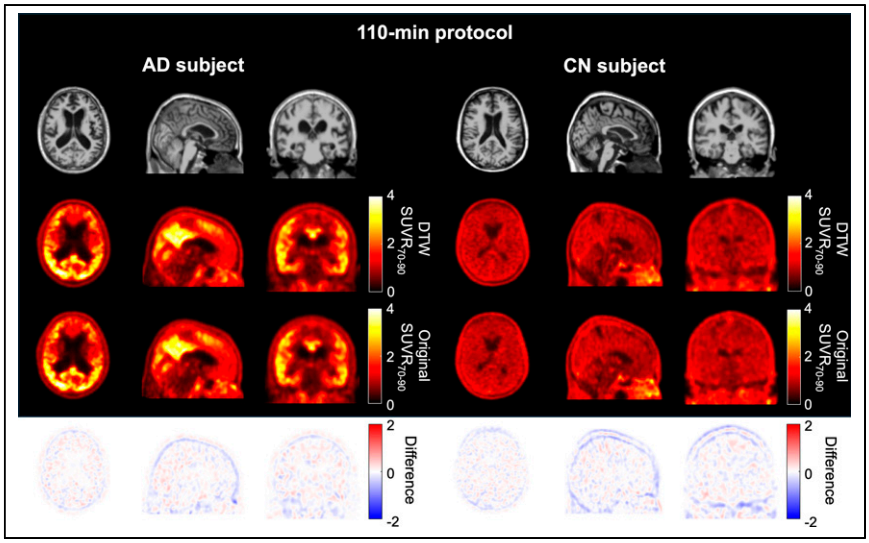

FIGURE 7. Model-based $SUVR_{70-90}$ maps computed for 60-min break with biexponential fit and 110-min scan analysis as well as corresponding MR structural images for same AD and CN subjects as shown in Figure 4. First row shows magnetization-prepared rapid gradient echo as anatomic reference. Second row shows parametric $SUVR_{70-90}$ images generated from DTW images. Third row shows original (i.e., from acquired data) $SUVR_{70-90}$ images for comparison. Fourth row shows images of difference ($SUVR_{70-90}$ DTW – $SUVR_{70-90}$ original).

range of [^{18}F]MK6240 brain kinetics, with corresponding regional DVRs reaching values of up to 5, thus allowing us to evaluate DTW protocols across a wide range of tau levels. Although we are confident that our findings would generalize well in a larger cohort, additional studies on AD subjects with high tau levels (i.e., brain regions with very slow kinetics) may help confirm the method's applicability in this clinical population. On the contrary, our T-RT analysis was limited to only 2 CN subjects, thus restricting the validity of our T-RT findings to low-binding regions. Moreover, ideally a greater number of participants would be needed to allow reliable and more conclusive T-RT calculations.

CONCLUSION

Our study demonstrated that a DTW dynamic protocol offers a practical and quantitatively accurate alternative to a full [^{18}F]MK6240 dynamic scan. The approach allows for both the quantification of tau burden and an index of cerebral perfusion while improving scanning efficiency and reducing patient discomfort compared with a full dynamic acquisition.

KEY POINTS

QUESTION: Can a DTW dynamic imaging protocol provide accurate quantitative measurements of tau burden with the second-generation tau tracer [^{18}F]MK6240?

PERTINENT FINDINGS: Robust and accurate quantitative measurements of tau were obtained using a DTW protocol with an optimal break of 60 min. Such a protocol offers a practical and quantitatively accurate alternative to a full [^{18}F]MK6240 dynamic scan.

IMPLICATIONS FOR PATIENT CARE: This approach enables the quantification of both tau and cerebral perfusion while reducing the total acquisition time compared with a full dynamic acquisition, making it suitable for a clinical setting.

DISCLOSURE

This study was funded by the Massachusetts General Hospital Thrall Innovation award (Nicolas Guehl) and by grants R21AG070714 (Nicolas Guehl), R01AG076153, P41EB022544 (Georges El Fakhri), and R01AG046396 (Keith Johnson). Rik Ossenkoppele has received research funding or support from the European Research Council, ZonMw, NWO, the National Institutes of Health, the Alzheimer Association, Alzheimer Nederland, Stichting Dioraphte, the Cure Alzheimer fund, Health Holland, ERA PerMed, Alzheimerfonden, Hjarnfonden, Avid Radiopharmaceuticals, Janssen Research & Development, Roche, Quanterix, and Optina Diagnostics; has given lectures in symposia sponsored by GE HealthCare; received speaker fees from Springer; and is an advisory board member for Asceneuron and a steering committee member for Biogen and Bristol Myers Squibb. All the aforementioned has been paid to his institutions. No other potential conflict of interest relevant to this article was reported.

ACKNOWLEDGMENTS

We thank Julia Scotton and Nicole DaSilva for preparing the subjects, scanning, and monitoring, and we thank Marina MacDonald-Soccorso for helping with data management.

REFERENCES

1. Walji AM, Hostetler ED, Selnick H, et al. Discovery of 6-(fluoro-^{18}*F*)-3-(*1H*-pyrrolo[2,3-*c*]pyridin-1-yl)isoquinolin-5-amine ([^{18}F]-MK-6240): a positron emission tomography (PET) imaging agent for quantification of neurofibrillary tangles (NFTs). *J Med Chem.* 2016;59:4778–4789.
2. Hostetler ED, Walji AM, Zeng Z, et al. Preclinical characterization of ^{18}F-MK-6240, a promising PET tracer for in vivo quantification of human neurofibrillary tangles. *J Nucl Med.* 2016;57:1599–1606.
3. Betthauser TJ, Cody KA, Zammit MD, et al. In vivo characterization and quantification of neurofibrillary tau PET radioligand ^{18}F-MK-6240 in humans from Alzheimer disease dementia to young controls. *J Nucl Med.* 2019;60:93–99.
4. Lohith TG, Bennacef I, Vandenberghe R, et al. Brain imaging of Alzheimer dementia patients and elderly controls with ^{18}F-MK-6240, a PET tracer targeting neurofibrillary tangles. *J Nucl Med.* 2019;60:107–114.
5. Pascoal TA, Shin M, Kang MS, et al. In vivo quantification of neurofibrillary tangles with [^{18}F]MK-6240. *Alzheimers Res Ther.* 2018;10:74.
6. Guehl NJ, Wooten DW, Yokell DL, et al. Evaluation of pharmacokinetic modeling strategies for in-vivo quantification of tau with the radiotracer [^{18}F]MK6240 in human subjects. *Eur J Nucl Med Mol Imaging.* 2019;46:2099–2111.
7. Aguero C, Dhaynaut M, Normandin MD, et al. Autoradiography validation of novel tau PET tracer [F-18]-MK-6240 on human postmortem brain tissue. *Acta Neuropathol Commun.* 2019;7:37.
8. Salinas C, Lohith TG, Purohit A, et al. Test-retest characteristic of [^{18}F]MK-6240 quantitative outcomes in cognitively normal adults and subjects with Alzheimer's disease. *J Cereb Blood Flow Metab.* 2020;40:2179–2187.
9. Fu JF, Lois C, Sanchez J, et al. Kinetic evaluation and assessment of longitudinal changes in reference region and extracerebral [^{18}F]MK-6240 PET uptake. *J Cereb Blood Flow Metab.* 2023;43:581–594.
10. Lois C, Fu JF, Salvatore AN, et al. Test–retest performance of [^{18}F]MK-6240 tau burden and relative delivery indices in cognitively normal older subjects using PET/MRI. *Imaging Neuroscience.* 2024;2:1–20.

11. van Dyck CH, Swanson CJ, Aisen P, et al. Lecanemab in early Alzheimer's disease. *N Engl J Med.* 2023;388:9–21.
12. Guehl NJ, Dhaynaut M, Hanseeuw BJ, et al. Measurement of cerebral perfusion indices from the early phase of [^{18}F]MK6240 dynamic tau PET imaging. *J Nucl Med.* 2023;64:968–975.
13. Fu JF, Juttukonda MR, Garimella A, et al. [^{18}F]MK-6240 radioligand delivery indices as surrogates of cerebral perfusion: bias and correlation against [^{15}O]water. *J Nucl Med.* 2025;66:410–417.
14. Hammes J, Leuwer I, Bischof GN, Drzezga A, van Eimeren T. Multimodal correlation of dynamic [^{18}F]-AV-1451 perfusion PET and neuronal hypometabolism in [^{18}F]-FDG PET. *Eur J Nucl Med Mol Imaging.* 2017;44:2249–2256.
15. Brendel M, Wagner L, Levin J, et al. Perfusion-phase [^{18}F]THK5351 tau-PET imaging as a surrogate marker for neurodegeneration. *J Alzheimers Dis Rep.* 2017; 1:109–113.
16. Beyer L, Nitschmann A, Barthel H, et al. Early-phase [^{18}F]PI-2620 tau-PET imaging as a surrogate marker of neuronal injury. *Eur J Nucl Med Mol Imaging.* 2020; 47:2911–2922.
17. Rodriguez-Vieitez E, Leuzy A, Chiotis K, Saint-Aubert L, Wall A, Nordberg A. Comparability of [^{18}F]THK5317 and [^{11}C]PIB blood flow proxy images with [^{18}F]FDG positron emission tomography in Alzheimer's disease. *J Cereb Blood Flow Metab.* 2017;37:740–749.
18. Meyer PT, Hellwig S, Amtage F, et al. Dual-biomarker imaging of regional cerebral amyloid load and neuronal activity in dementia with PET and ^{11}C-labeled Pittsburgh compound B. *J Nucl Med.* 2011;52:393–400.
19. Peretti DE, Vallez Garcia D, Reesink FE, et al. Relative cerebral flow from dynamic PIB scans as an alternative for FDG scans in Alzheimer's disease PET studies. *PLoS One.* 2019;14:e0211000.
20. Carson RE, Channing MA, Blasberg RG, et al. Comparison of bolus and infusion methods for receptor quantitation: application to [^{18}F]cyclofoxy and positron emission tomography. *J Cereb Blood Flow Metab.* 1993;13:24–42.
21. Slifstein M. Revisiting an old issue: the discrepancy between tissue ratio-derived binding parameters and kinetic modeling-derived parameters after a bolus of the serotonin transporter radioligand ^{123}I-ADAM. *J Nucl Med.* 2008;49:176–178.
22. van Berckel BN, Ossenkoppele R, Tolboom N, et al. Longitudinal amyloid imaging using ^{11}C-PiB: methodologic considerations. *J Nucl Med.* 2013;54:1570–1576.
23. Lammertsma AA. Forward to the past: the case for quantitative PET imaging. *J Nucl Med.* 2017;58:1019–1024.
24. Jack CR, Jr, Bennett DA, Blennow K, et al. A/T/N: an unbiased descriptive classification scheme for Alzheimer disease biomarkers. *Neurology.* 2016;87: 539–547.
25. Jack CR Jr, Bennett DA, Blennow K, et al. NIA-AA research framework: toward a biological definition of Alzheimer's disease. *Alzheimers Dement.* 2018;14:535–562.
26. Jack CR Jr, Andrews JS, Beach TG, et al. Revised criteria for diagnosis and staging of Alzheimer's disease: Alzheimer's Association Workgroup. *Alzheimers Dement.* 2024;20:5143–5169.
27. Bullich S, Barthel H, Koglin N, et al. Validation of noninvasive tracer kinetic analysis of ^{18}F-Florbetaben PET using a dual-time-window acquisition protocol. *J Nucl Med.* 2018;59:1104–1110.
28. Heeman F, Yaqub M, Lopes Alves I, et al.; AMYPAD Consortium. Optimized dual-time-window protocols for quantitative [^{18}F]flutemetamol and [^{18}F]florbetaben PET studies. *EJNMMI Res.* 2019;9:32.
29. Wang Z, Wu Y, Li X, et al. Comparison between a dual-time-window protocol and other simplified protocols for dynamic total-body ^{18}F-FDG PET imaging. *EJNMMI Phys.* 2022;9:63.
30. Tuncel H, Visser D, Yaqub M, et al. Effect of shortening the scan duration on quantitative accuracy of [^{18}F]flortaucipir studies. *Mol Imaging Biol.* 2021;23:604–613.
31. Kolinger GD, Vallez Garcia D, Lohith TG, et al. A dual-time-window protocol to reduce acquisition time of dynamic tau PET imaging using [^{18}F]MK-6240. *EJNMMI Res.* 2021;11:49.
32. Albert MS, DeKosky ST, Dickson D, et al. The diagnosis of mild cognitive impairment due to Alzheimer's disease: recommendations from the National Institute on Aging-Alzheimer's Association workgroups on diagnostic guidelines for Alzheimer's disease. *Alzheimers Dement.* 2011;7:270–279.
33. Johnson KA, Schultz A, Betensky RA, et al. Tau positron emission tomographic imaging in aging and early Alzheimer disease. *Ann Neurol.* 2016;79:110–119.
34. Pan T, Einstein SA, Kappadath SC, et al. Performance evaluation of the 5-ring GE Discovery MI PET/CT system using the National Electrical Manufacturers Association NU 2-2012 standard. *Med Phys.* 2019;46:3025–3033.
35. Collier TL, Yokell DL, Livni E, et al. cGMP production of the radiopharmaceutical [^{18}F]MK-6240 for PET imaging of human neurofibrillary tangles. *J Labelled Comp Radiopharm.* 2017;60:263–269.
36. Wilson AA, Garcia A, Chestakova A, Kung H, Houle S. A rapid one-step radiosynthesis of the β-amyloid imaging radiotracer N-methyl-[^{11}C]2-(4′-methylaminophenyl)-6-hydroxybenzothiazole ([^{11}C]-6-OH-BTA-1). *J Labelled Comp Radiopharm.* 2004;47:679–689.
37. Fischl B. FreeSurfer. *Neuroimage.* 2012;62:774–781.
38. Logan J, Fowler JS, Volkow ND, Wang GJ, Ding YS, Alexoff DL. Distribution volume ratios without blood sampling from graphical analysis of PET data. *J Cereb Blood Flow Metab.* 1996;16:834–840.
39. Gogola A, Minhas DS, Villemagne VL, et al. Direct comparison of the tau PET tracers ^{18}F-flortaucipir and ^{18}F-MK-6240 in human subjects. *J Nucl Med.* 2022;63:108–116.
40. Alosco ML, Mejia Perez J, Culhane JE, et al. ^{18}F-MK-6240 tau PET in patients at-risk for chronic traumatic encephalopathy. *Mol Neurodegener.* 2025;20:23.
41. Slifstein M, Laruelle M. Effects of statistical noise on graphic analysis of PET neuroreceptor studies. *J Nucl Med.* 2000;41:2083–2088.